Manganite charge and orbitally ordered and disordered states probed by Fe substitution into Mn site in LnBaMn$_{1.96}$Fe$_{0.04}$O$_5$, LnBaMn$_{1.96}$Fe$_{0.04}$O$_6$ and LnBaMn$_{1.96}$Fe$_{0.04}$O$_{5.5}$ (Ln = Y, Gd, Sm, Nd, Pr, La)

Alexandre I. Rykov [a,b,*], Yutaka Ueda [b], Kiyoshi Nomura [a]

[a] School of Engineering, The University of Tokyo, Hongo 7-3-1, 113-8656, Japan
[b] Institute for Solid State Physics, University of Tokyo, 5-1-5 Kashiwanoha, Kashiwa, Chiba 277-8581, Japan

ARTICLE INFO

ABSTRACT

The layered manganese oxides LnBaMn$_{1.96}$Fe$_{0.04}$O$_y$ (Ln = Y, Gd, Sm, Nd, Pr, La) have been synthesized for $y = 5, 5.5$ and 6. In the oxygen-saturated state ($y = 6$) they exhibit the charge and orbital order at ambient temperature for Ln = Y, Gd, Sm, but unordered e_g-electronic system for Ln = La, Pr, Nd. Fourfold increase of quadrupole splitting was observed owing to the charge and orbital ordering. This is in agreement with the jumplike increase in distortion of the reduced perovskite-like cell for the charge and orbitally ordered manganites compared to the unordered ones. Substitution of 2% of Mn by Fe suppresses the temperatures of structural and magnetic transitions by 20–50 K. Parameters of the crystal lattices and the room-temperature Mössbauer spectra were studied on 40 samples whose structures were refined within five symmetry groups: $P4/mmm$, $P4/nmm$, Pm-3m, Icma and $P2/m$. Overwhelming majority of the Fe species are undifferentiated in the Mössbauer spectra for most of the samples. Such the single-component spectra in the two-site structures are explained by the preference of Fe towards the site of Mn(III) and by the segmentation of the charge and orbitally ordered domains.

© 2009 Elsevier Inc. All rights reserved.

1. Introduction

The manganites LnBaMn$_2$O$_y$ ($y = 5$ and 6, Ln = Y and rare-earth elements) compose a novel family of oxides with the layered structures derived of perovskite via unmixing the Ln and Ba cations from the *A*-site into separate layers [1–3]. The layered structures for the oxygen contents $y = 6$ and 5 differ by one layer, which is, respectively, LnO and Ln□, with □ standing for vacant oxygen site. Both these structures enclose the ions of manganese in the states of half-doping mixed valence. The Jahn-Teller (JT) ions Mn^{3+} are involved into the planar checkerboard arrangements either with Mn^{2+} or with Mn^{4+} ions for $y = 5$ and 6, respectively. The layered arrangement of Ln (III) and Ba(II) generates on Mn^{3+} cations the staggered systems of either the out-of-plane d$_{z^2}$ orbitals ($y = 5$) or the in-plane d$_{3x^2-r^2}$/d$_{3y^2-r^2}$ orbitals ($y = 6$). The charge ordering between Mn^{3+} and Mn^{2+}(Mn^{4+}) and orbital ordering between d$_{z^2}$ (d$_{3x^2-r^2}$ and d$_{3y^2-r^2}$) are typically coupled into a bound process giving birth to the charge–orbitally ordered state denoted hereof as COO.

There occur within a family of the ordered manganites several ways of stacking these e_g-electronic sheets into the 3D COO structures [4,5].

On the other hand, the oxygen content $y = 5.5$ yields the single-valence Mn(III) system with no charge differentiation, but with the order of the Mn^{3+} orbits related to the ordered system of the oxygen vacancies [6,7]. The manganite LnBaMn$_2$O$_{5.5}$ encloses the JT Mn^{3+} ions in the equipopulated pyramidal and octahedral coordinations. The pyramids and octahedra form the chains, in which the orbital order consists of the alternating parallel and perpendicular to the chains d$_{x^2}$ and d$_{z^2}$ orbitals filled in octahedra and in pyramids, respectively.

In this work, we employ the Mössbauer spectroscopy to explore the variety of the structural and chemical states adopted by the Fe impurity doped into the Mn sites for the ordered structures corresponding to $y = 5, 5.5$ and 6. For $y = 6$, in addition to the *A*-site ordered layered structures, the cubic disordered Fe-doped systems were also synthesized. We show that the phase transition succession in LnBaMn$_{1.96}$Fe$_{0.04}$O$_6$ remains quite resembling to that in undoped LnBaMn$_2$O$_6$.

Mössbauer spectroscopy senses the local surrounding of the probe nuclei (^{57}Fe in our case) substituted into Mn sites through observing the electric field gradient (EFG) and magnetic hyperfine fields generated by adjacent electrons. Based on interpreting these quantities our study reveals the way by which the impurity ion

---

controls the composition of its surrounding. In the charge-ordered state, only one component Fe(III) is displayed in Mössbauer spectra. The apparent controversy between the singular Fe^{3+} states and the persistent COO of Mn^{2+}/Mn^{3+} in $LnBaMn_{1.96}$ $Fe_{0.04}O_5$ and of Mn^{3+}/Mn^{4+} in $LnBaMn_{1.96}Fe_{0.04}O_6$ can be resolved supposing that the Fe dopants break the long range COO and shorten the COO correlation lengths.

Three groups of the oxygen-saturated manganites were specified previously according to the size of Ln [8] as Ln(first) = (La, Pr, Nd), Ln(second) = (Sm, Eu, Gd) and Ln(third) = (Y, Tb, Dy, Ho). A few members from each of these families were investigated in this work for the effect of the Fe species on the transitions manifested in magnetic properties. It was shown in several previous works [9,10] that besides the A-site disordered and fully ordered systems the partly A-site ordered layered manganites can also be prepared in special conditions. In this work, we avoided making the partially A-site ordered samples. Our samples were stoichiometric and having an integer or half-integer oxygen index except a few samples among the A-site disordered systems ([Ar-2] samples), as discussed below.

2. Experimental

The manganites $LnBaMn_{1.96}Fe_{0.04}O_y$ were prepared for Ln = Y, Gd, Sm, $(Sm_{0.9}Nd_{0.1})$, $(Sm_{0.1}Nd_{0.9})$, Nd, Pr and La. The oxides Fe_2O_3 and Ln_2O_3 (Pr_6O_{11} for Pr-based manganites) were mixed with the carbonates $BaCO_3$ and $MnCO_3$. The mixtures were first annealed in 6 N pure Ar (99.9999%) flow at 1350 °C. Rapid cooling from this temperature in Ar has led to obtaining the oxygen-depleted phases $LnBaMn_{1.96}Fe_{0.04}O_5$. A fraction of each sample was picked out and denoted as [Ar-1]. Remaining part of a sample was subjected to further thermal treatments.

Five protocols of thermal treatment were applied. Sequentially, after each annealing step a fraction of the sample was picked out, and the remaining part of the sample was subjected to the next step. Five series of the samples were obtained in this way. In Table 1, they correspond to columns labeled as [Ar-1], [O-1], [Dis-O], [Ar-2] and [O-2] according to the final annealing step. Eight rows of Table 1 correspond to a particular rare-earth Ln. In

total, 40 (5 × 8) samples were analyzed. All the samples of series [Ar-1], [O-1], and most of the samples from the [Ar-2] and [O-2] series showed single-phase X-ray patterns (Fig. 1). Only a few samples among the [Ar-2] and [O-2] series showed the presence of a second phase. Members of the [Dis-O] series were all cubic single-phase, except the Y-based sample. The latter consisted of binary hexagonal oxides $YMnO_3$ (PDF 25-1079) and $BaMnO_3$(PDF 14-274), and contained no perovskite phase.

Lattice parameters were refined through the analysis of full-profile X-ray diffraction intensities using FULLPROF program [11,12]. The data were obtained by means of a "Mac Science" diffractometer using the Cu$-K\alpha$ radiation ($\lambda = 0.15405$ and 0.15443 nm). Parameters of preferred orientation of platy crystal-lites along the axis [001] were refined using March–Dollase function [13].

Measurements of magnetization were performed using a SQUID magnetometer in an applied field of 1 kOe at heating the samples from 5 K to T_{max} and then at cooling from $T = T_{max}$ down to 5 K. This measurement protocol was applied in $LnBaMn_{1.96}$ $Fe_{0.04}O_6$ for Ln = Sm with $T_{max} = 400$ K and for Ln = $(Nd_{0.9}Sm_{0.1})$ with $T_{max} = 370$ K. The magnetization in $YBaMn_{1.96}Fe_{0.04}O_6$ was measured first at heating from ambient temperature to $T_{max} = 600$ K (Ln = Y) and then at cooling from $T = T_{max}$ down to 5 K. The sample was then remagnetized at 5 K by setting the external field $H = 0 \pm 0.01$ kOe followed by reapplying $H = 1$ kOe. Finally, this sample magnetization was measured at heating up to 300 K.

Mössbauer spectra were measured at room temperature and at 11 K. Isomer shifts are referred relatively α-Fe.

3. Results and discussion

The rest of this article is organized as follows. First, the structure of the samples obtained is described following the sequence of thermal treatments [Ar-1], [O-1], [Dis-O], [Ar-2], and [O-2]. It will be shown that the Ln's are grouped into three groups according to the behaviors of the Ln-based samples for some of these treatments. Second, these three groups will be characterized by their Mössbauer spectra.

Table 1
Symmetry modifications of $LnBaMn_{1.96}Fe_{0.04}O_y$ (Ln = Y and rare earths from La to Gd) best suited to our X-ray diffraction data according to their Rietveld analysis.

Anneal step no.	1	2	3	4	5
Gas	Ar(5 N)	O_2	95%O_2	Ar(5 N)	O_2
T (°C)	1350	500	1400	1450	350
Time (h)	48	48	24	24	100
Steps	1	1, 2	1, 2, 3	1, 2, 3, 4	1, 2, 3, 4, 5
Sample	[Ar-1]	[O-1]	[Dis-O]	[Ar-2]	[O-2]
La	$P4/nmm$	$P4/mmm$	$Pm\bar{3}m$	$Pm\bar{3}m$	$Pm\bar{3}m$
Pr	$P4/nmm$	$P4/mmm$	$Pm\bar{3}m$	$Pm\bar{3}m$	$Pm\bar{3}m$
Nd	$P4/nmm$	$P4/mmm$	$Pm\bar{3}m$	$Pm\bar{3}m$	$Pm\bar{3}m$
$Sm_{0.1}$, $Nd_{0.9}$	$P4/nmm$	$P4/mmm$	$Pm\bar{3}m$	$Pm\bar{3}m$	$Pm\bar{3}m$
$Sm_{0.9}$, $Nd_{0.1}$	$P4/nmm$	$P4/mmm$	$Pm\bar{3}m$	Icma(96%) + $P4/nmm$(4%)	$P4/mmm$(56%), $P4/mmm$(44%)
Sm	$P4/nmm$	$P4/mmm$	$Pm\bar{3}m$	Icma(93%) + $P4/nmm$(7%)	$P4/mmm$(51%), $P4/mmm$(49%)
Gd	$P4/nmm$	$P4/mmm$	$Pm\bar{3}m$	Icma(89%) + $P4/nmm$(11%)	$P4/mmm$
Y	$P4/nmm$	$P\bar{1}$	Binary oxides	Icma	$P\bar{1}$

Sequence of annealing steps applied to synthesize these modifications consisted of a number of gas-heat treatments. Their conditions are shown in the upper rows. The annealing steps were applied sequentially. After each step a fraction of sample was picked out. The fractions labeled [Ar-1], [O-1], [Dis-O], [Ar-2] and [O-2] were obtained after the steps 1–5, respectively. Several samples among the [Ar-2] and [O-2] series showed a presence of second phase. In these cases, the percentage of phases provided by FULLPROF program is given.

Sm0.9Nd0.1BaMn1.96Fe0.04Oy
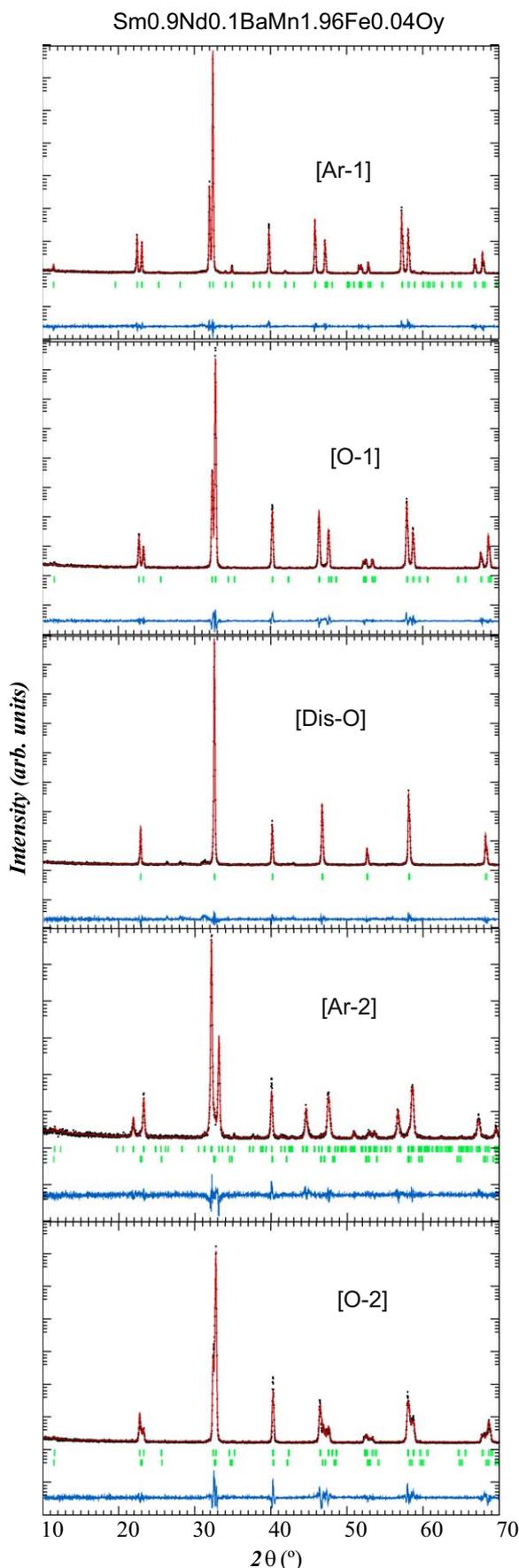
Fig. 1. X-ray diffraction patterns of $Sm_{0.9}Nd_{0.1}BaMn_{1.96}Fe_{0.04}O_y$, obtained by thermal treatments [Ar-1], [O-1], [Dis-O], [Ar-2] and [O-2] explicated in Table 1. Dots represent the observed profiles; solid lines represent calculated profiles and difference.

3.1. Structural considerations: phases and phase transitions from X-ray diffraction and magnetization

Three groups of manganites specified previously according to the size of Ln [8] show a distinct behavior with respect to the thermal treatments at the steps 3–5, as is illustrated by our Table 1. Because we used for the synthesis of the [Ar-1], [O-1] and [Dis-O] series the conditions similar to previously reported [2,6,3], we may attribute three groups of different behaviors in Table 1 not only to Fe-doped, but also to clean undoped manganites. Stability of the cubic disordered phase $Pm\overline{3}m$ turns out to depend on the size of Ln.

3.1.1. Oxygen-depleted layered $LnBaMn_{1.96}Mn_{0.04}O_5$

We observed that all of our X-ray profiles from "O_5" samples are perfectly fitted with the $P4/nmm$ model (Fig. 2b). The quality of fit was declining when we attempted to fit the patterns in terms of $P4/mmm$ model (Fig. 2a). This fact is suggestive of persistent charge order which remains undefeated by the current level of Fe doping. In the pure $LaBaMn_2O_5$, the COO between Mn^{2+} and Mn^{3+} was initially required from the occurrence of the supercell extra reflections in electron diffraction patterns [2]. In X-ray profiles, we see only a minor evidence of COO in the improvement of R-factors for the $P4/nmm$ model. Notable improvement was observed for every Ln.

Comparing the parameters of lattice cell depending on Ln, it is convenient to plot them in function of the volume V_r of the reduced cell, i.e., perovskite cell (Fig. 2d). It is shown in Fig. 3 that the lattice parameters in $LaBaMn_2O_5$ vary monotonically as the volume of the reduced cell increases with increasing the size of Ln. Distortion of the reduced cell can be calculated in $LnBaMn_2O_5$ as $D_5 = 2(a/\sqrt{2} - c/2)/(a/\sqrt{2} + c/2)$. From Y to La the distortion decreases from 2.56% to 2.36%, respectively.

3.1.2. Oxygen-saturated layered $LnBaMn_{1.96}Mn_{0.04}O_6$

In contrast to the oxygen-depleted phase, the variation of parameters of the oxygen-saturated phase vs. V_r is non-monotonic. Considering the distortion of reduced cell $D_6 = 2(a - c/2)/(a + c/2)$ two regions on the V_r-axis can be distinguished with $D_6 \approx 2.5\%$ in the region of small V_r and $D_6 \sim 0.7$–0.4% for larger V_r (Fig. 3). The border between two regions is the same that divides the Table 1 according to the products of the treatments [Ar-2] and [O-2].

Contrarily to the case of $y = 5$ the quality of X-ray Rietveld refinement was not improvable with using the enlarged cell $2a_p \times 2a_p \times 2a_p$. The tetragonal cell $a_p \times a_p \times 2a_p$ (Fig. 2c) suits best to all the samples in the layer-ordered oxygen-saturated family, with one exception of $YBaMn_{1.96}Fe_{0.04}O_6$. The structure of the latter was refined using the triclinic symmetry (space group $P\overline{1}$ no.2). Previously, the structure of $YBaMn_2O_6$ was described first by the monoclinic symmetry (group $P2$ no.3) [4], however, a recent high resolution diffraction study [14] revealed a triclinic distortion, so that the use of the space group $P\overline{1}$ is more appropriate, although the resolution in our profiles was insufficient to confirm the triclinic symmetry. In fact, our refinements in the Fe-doped samples could not give any preference to one of the $P\overline{1}$, $P2$ groups.

In members of each of three groups of manganites, as we grouped them by the size of Ln in Table 1, a succession of phase transitions was observed via the magnetization jumps and humps (Fig. 4). These features are roughly same as in undoped manganites, but differ in details. In $YBaMn_{1.96}Fe_{0.04}O_6$ and $SmBaMn_{1.96}Fe_{0.04}O_6$, the highest in temperature jump of magnetization is associated with the structural transition, which is triclinic-to-monoclinic for Ln = Y
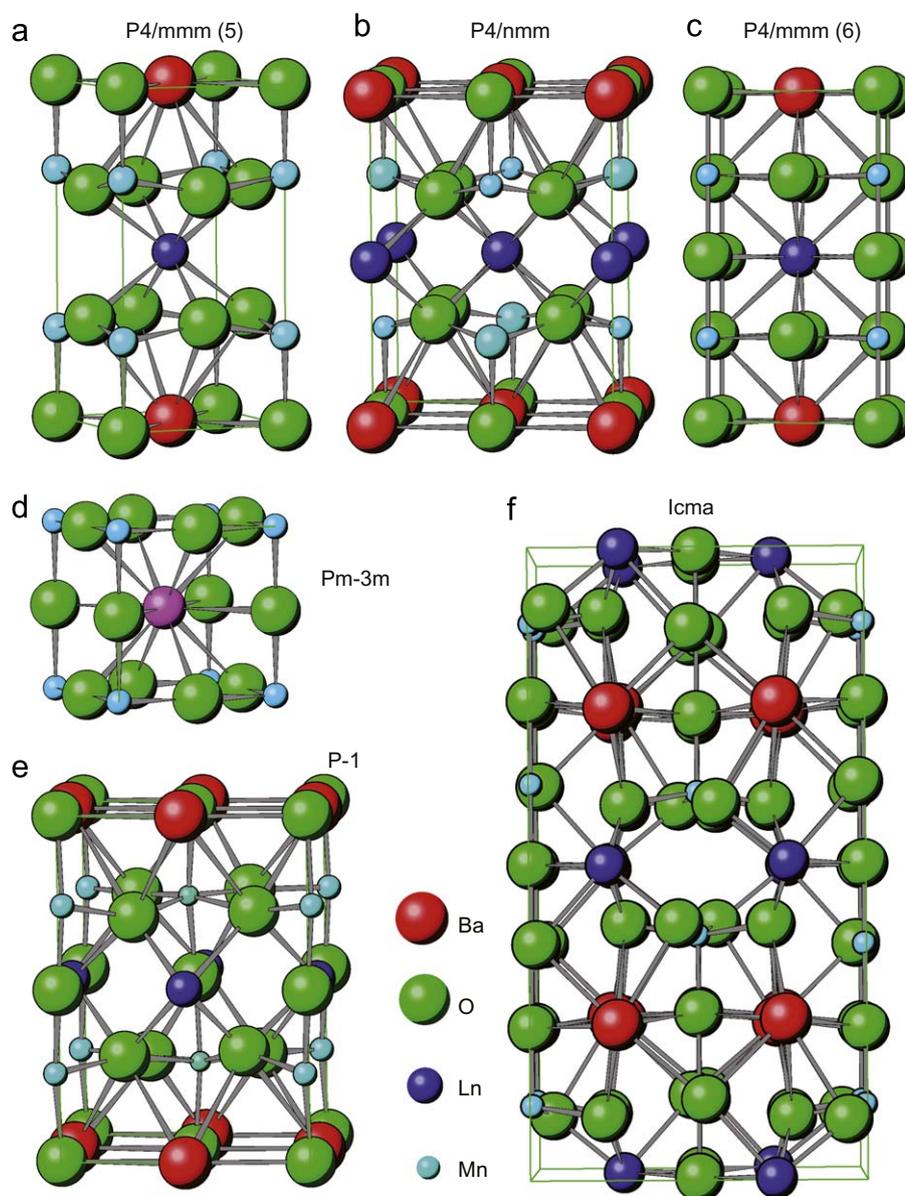
Fig. 2. The crystal structures and symmetry groups employed in Rietveld analysis of X-ray diffraction profiles for layer-ordered $LnBaMn_2O_5$ (a, b), $LnBaMn_2O_6$ (c), disordered $Ln_{0.5}Ba_{0.5}MnO_3$ (d), $YBaMn_2O_6$ (e), and $LnBaMn_2O_{5.5}$ (f). Here $Ln = La$, Pr, Nd ($Nd_{0.9}Sm_{0.1}$), ($Nd_{0.1}Sm_{0.9}$), Sm and Gd.

[14], and tetragonal-to-orthorhombic for $Ln = Sm$ [15]. Orbital ordering is now believed [16] to accompany these structural transition ($T = T_t$), while the complete charge ordering temperature is attributed [3,4], to a separate small hump shifted from T_t to lower temperature by Δ_t. In $YBaMn_{1.96}Fe_{0.04}O_6$, for example $\Delta_t \approx 40$ K. In the undoped manganite, the temperature of charge ordering $T_{CO} = T_t - \Delta_t$ is associated with the sharp localization of charge carriers. In the magnetization of $YBaMn_{1.96}Fe_{0.04}O_6$, the large jump is observed without any small foregoing hump. Interestingly, similar disappearance of the hump in magnetization caused by Fe doping was reported for the orbital ordering transition in $BiMnO_3$ [17]. In a similar way, the transition is smeared in our Fe-doped samples, and the magnetization hump is suppressed by the Fe substitution.

Another key feature of the doped systems stems from the fact that the values of T_t are slightly suppressed compared to those in the undoped $YBaMn_2O_6$ and $SmBaMn_2O_6$ [4,9]. The suppression ranges ΔT_t (2% Fe) are of 50 and 40 K for $Ln = Y$ and Sm, respectively.

Despite of the similarity of the values of ΔT_t, there occurs a large difference between the cases of $Ln = Y$ and Sm for the shift of the transition temperature with the reversal of the temperature sweep direction. Such a shift is associated with an energy barrier for nucleation of a new phase within the region of overheating or undercooling the preceding phase. The hysteresis indicates strongly the first-order character of transition that was observed also in undoped $YBaMn_2O_6$ [4]. The large nucleation barrier is observed in $YBaMn_2O_6$ but not in $SmBaMn_2O_6$. This is in agreement with a very small structural distortion in $SmBaMn_2O_6$ at T_t as reported by Akahoshi et al. [15].

Temperatures of Neel (T_N) are also notably suppressed for both cases of $Ln = Y$ and Sm, as well as for $Nd_{0.9}Sm_{0.1}BaMn_{1.96}Fe_{0.04}O_6$. The antiferromagnetic transitions humps were observed [18,9] at 290 and 250 K in the undoped $NdBaMn_2O_6$ and $SmBaMn_2O_6$, respectively, therefore, the T_N value of 286 K is expected for the solid solution $Nd_{0.9}Sm_{0.1}BaMn_2O_6$. Remaining suppression $\Delta T_N \simeq 10$ K should be attributed to the effect of Fe substitution.
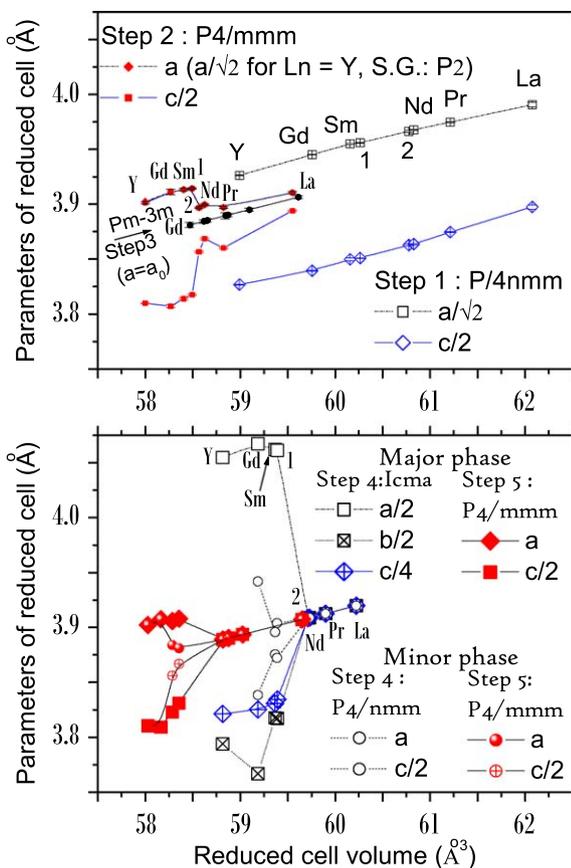
Fig. 3. Lattice parameters of the reduced perovskite-like cell vs. volume of this cell in 2% Fe-doped manganites. Phases obtained through thermal treatments [Ar-1] (step 1), [O-1] (step 2), and [Dis-O] (step 3) are presented in upper panel. In the same ranges, phases obtained through thermal treatments [Ar-2] (step 4) and [O-2] (step 5) are presented in lower panel. Lattice parameters in two-phase samples are plotted vs. average cell volume, taking into account the refined percentage of each phase. Mixed-rare-earths manganites $Sm_{0.9}Nd_{0.1}BaMn_{1.96}Fe_{0.04}O_y$ and $Sm_{0.1}Nd_{0.9}BaMn_{1.96}Fe_{0.04}O_y$ are denoted by "1" and "2", respectively. In $YBaMn_{1.96}Fe_{0.04}O_6$ the parameters of the reduced cell are obtained with the space group $P2$ and corresponding monoclinic angle $\beta = 90.296°$ was taken into account in the calculation of the reduced cell volume.

Temperature ranges for sweep-reversal hysteresis around T_N are not much different between the three.

3.1.3. Oxygen-saturated isotropic $Ln_{0.5}Ba_{0.5}Mn_{0.98}Fe_{0.02}O_3$

According to the Table 1, the disordered phase was obtained in this work from the ordered one, after the thermal treatment at 1400 °C in the flowing gas mixture of 95% of O_2 and 5% of Ar. From the synthesis reported previously [19] our method differed thus by the precursor and gave the same cubic phases for all Ln's except Y. Only the Y-based complex manganite has decomposed into binary manganites by this high-temperature oxygenating treatment. Irrespective of Ln, such a heat treatment was destructive for the layered arrangement of Ln and Ba formed at the first [Ar-1] step, and resulted either in isotropic homogeneous distribution of Ln and Ba, or in their separation for Ln = Y.

A half among eight compositions studied (in upper part of Table 1) showed a reduced stability of the disordered phase $Ln_{0.5}Ba_{0.5}Mn_{0.98}Fe_{0.02}O_3$ with respect to a subsequent oxygen-depletion treatment. The lower stability of the disordered manganites with small Ln correlates with the poorer perovskite tolerance factor. It is shown in Fig. 3 that the lattice parameters for the $Pm\overline{3}m$ phases [Ar-2] obtained after the step 4 are larger than
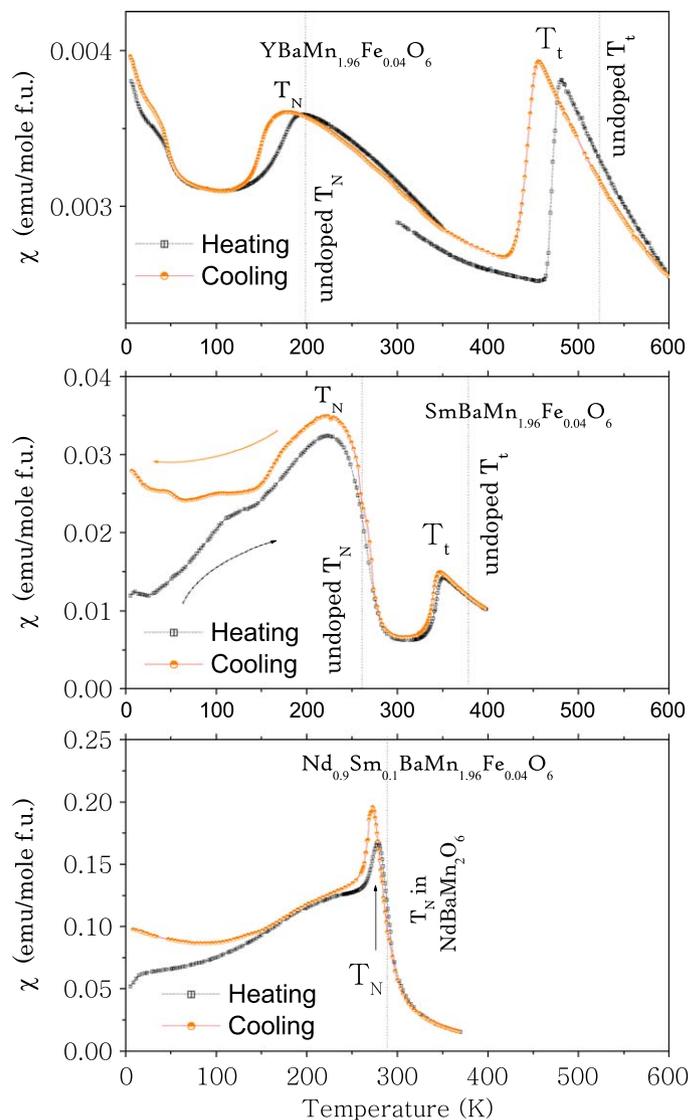
Fig. 4. Magnetic susceptibility M/H measured in the external field H of 1 kOe in $LnBaMn_{1.96}Fe_{0.04}O_6$ for Ln = Y, Sm and $(Nd_{0.9}Sm_{0.1})$. The zero-field-cooled magnetization was measured at heating the samples up to T_{max} of 600 K (Ln = Y), 400 K (Ln = Sm) and 370 K (Ln = $Nd_{0.9}Sm_{0.1}$) and then at cooling from $T = T_{max}$. Temperatures of phase transitions in pure (undoped) manganites indicated by vertical lines are from previous works [4,9].

those for the $Pm\overline{3}m$ phases [Dis-O] obtained after the step 3. The differences Δa are 0.013, 0.018, and 0.019 Å for Ln = La, Pr, and Nd, respectively. Increasing Δa indicates the increasing oxygen loss at the step 4. In the [Ar-2] samples, the oxygen index decreases from La to Nd and approaches the value of 2.75 near the border separating $Pm\overline{3}m$ and Ima2 phases. This is in agreement with the single-phase [Ar-2] sample of $Sm_{0.9}Nd_{0.1}BaMn_{1.96}Fe_{0.04}MnO_{5.5}$.

3.1.4. Intermediate-oxygen $LnBaMn_{1.96}Mn_{0.04}O_{5.5}$

The Ima2 phase contains layers BaO and $YO_{0.5}$ and the 1D channels are formed in the $YO_{0.5}$ layer (Fig. 2f). In several of the [Ar-2] samples the second phase (fully oxygen-depleted $LnBaMn_{1.96}Mn_{0.04}O_5$) appears because the Ima2 structure does not accommodate any oxygen deficiency. There appears to exist a miscibility gap between the "$O_{5.5}$" and "O_5" phases for the Ln in the lower half of the Table 1.

Distortion of the reduced cell can be described by the out-of-plane and in-plane parameters, having their origins in the layered

ordering of Ln and Ba and the chainlike ordering of oxygen atoms, respectively. The out-of-plane distortion $D_{5.5} = 2(a/4 + b/4 - c/4)/(a/4 + b/4 + c/4)$ is just slightly larger than D_5 and D_6. We obtained for Ln = Gd $D_{5.5} = 2.77\%$ roughly similar to D_5 and D_6. The in-plane parameter is the orthorhombicity of the reduced cell $D_o = 2(a/2 - b/2)/(a/2 + b/2)$. For Ln = Gd we obtained $D_o = 6.91\%$, which is much larger than $D_{5.5}$.

3.1.5. Additional oxygenating thermal treatment [O-2]

The final thermal treatment [O-2] conducted in oxygen gas flow at rather low temperature (350 °C) evidences a peculiar COO-melted phases obtained via oxygen loading into SmBaMn$_{1.96}$Fe$_{0.04}$O$_{5.5}$ and Sm$_{0.9}$Nd$_{0.1}$BaMn$_{1.96}$Fe$_{0.04}$O$_{5.5}$. In the group Ln = La, Pr and Nd, the lattice parameters before step 4 and after step 5 coincided (Fig. 3). Also, for Ln = Y and Gd one observes (Fig. 3) that both lattice parameters after step 5 have regained the values which they had before the step 4. On the other hand, neither [O-1] nor [Dis-O] X-ray patterns were restituted after the step 5 for Ln = Sm and Ln = (Sm$_{0.9}$Nd$_{0.1}$). As a matter of fact, the reoxygenation of [Ar-2] samples for these Ln's resulted in the two phase systems with approximately equal abundance of each phase. The X-ray profile refined with two *P*4/*mmm* phases gave us the parameters of these phases. For one of the phases they coincided with the parameters of the [O-1] phase, and for the other phase the distortion D_6 was as small as the distortion in the [O-1] phases for Ln = La, Pr, and Nd. We interpret the latter as the quenched COO-melted phase and it is confirmed further below via our Mössbauer study.

3.2. Mössbauer study

In agreement with the structure differences described above among three groups of Ln-based manganites, our Mössbauer study also reveals the characteristic features in each group. Hereafter, these groups are specified as La-group, Sm-group and Y-group.

3.2.1. La-group of Ln's

The characteristic feature of Mössbauer spectra in the [Ar-1] samples ("O$_5$"-phase, *P*4/*nmm*) is the two-doublet envelope of the spectra. We observe that the occurrence of two crystallographic sites in this phase for the largest Ln is sensed by the Fe probe. Both sites accommodate iron in the state of Fe(III). The ratio of the doublet areas is 7:3 (Fig. 5, top) instead of 5:5 expected for the random distribution of Fe over two sites. This indicates the iron preference towards one of these sites. The temperature at which the charge–orbital order sets in is too low to activate the migration of iron between the Mn(III) and Mn(II) sites. Therefore, we believe that the dopant species control the in-plane arrangement of the charges and orbitals at the surrounding ions of Mn. This becomes possible with decreasing the size of the ordered domain, especially when the COO correlation length becomes comparable to the average distance between the Fe dopants. The size of the Mn(II) site is too large for the Fe^{3+} ion; therefore, the Fe^{3+} species tend to escape to the smaller site of Mn(III). This results in the formation of a static or dynamic configuration of charge-ordered domains, which accommodate the majority of the Fe^{3+} dopants into the Mn(III) site surrounded by four next-neighboring (NN) Mn^{2+} species through the in-plane linkage and by one NN Mn^{3+} through the pyramid apex. Less obvious is the assignment of the secondary doublet can that be attributed either to Mn(II) site, or to a boundary domain site, surrounded in-plane by both Mn^{3+} and Mn^{2+}.

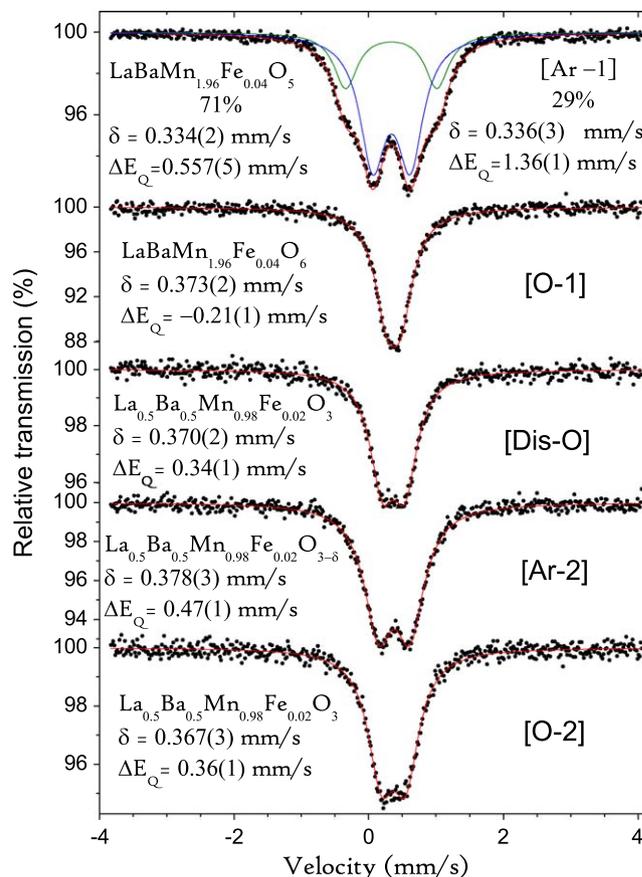Quadrupole splittings ΔE_Q of these two doublets are in agreement with our assignment. From the Mössbauer studies in

Fig. 5. Room-temperature Mössbauer spectra of LaBaMn$_{1.96}$Fe$_{0.04}$O$_6$ obtained by the sequential [Ar-1], [O-1], [Dis-O], [Ar-2] and [O-2] thermal treatments. The conditions of each step are shown in Table 1.

cuprates [20] it is known that the Fe^{3+} ions doped into the pyramidal site are shifted by u from the base of the pyramid towards its apex with u much larger for the Fe dopants than for the host JT ions. When the Fe^{3+} ions were the host ions instead of the impurities then the displacement parameter u was also much larger in the FeO$_5$ pyramid than in the CuO$_5$ pyramid [21,22]. Such an excessive displacement equalizes the in-plane and the out-of-plane bonds of the Fe^{3+} ions and results in strong reduction of the splitting ΔE_Q compared to its value expected from the ionic point charge model for the original pyramidal site of a JT ion [20]. We observe for the major doublet in the [Ar-1] sample of LnBaMn$_{1.96}$Mn$_{0.04}$O$_5$ that both the splitting $\Delta E_Q = 0.56$ mm/s and the chemical shift $\delta = 0.33$ mm/s are quite similar to ΔE_Q and δ of Fe-doped into Cu(2)-plane of YBa$_2$Cu$_3$O$_{7-x}$ [20,23,24]. This is consistent with our assignment of this doublet to the site of JT ion Mn^{3+}.

Minor doublet has a similar isomer shift, but ΔE_Q as large as 1.36 mm/s. Assignment of this ΔE_Q to the site of Mn(II) is plausible because this site is too large for Fe^{3+}, first of all, in equatorial dimension [2,25]. Embedded in such a site Fe^{3+} cation would distort its environment or move into an asymmetric position with large ΔE_Q. An alternative assignment of this doublet, which cannot be disregarded, is a special site, located on the interface between two charge-ordered domains.

In the oxygen-saturated [O-1] sample, we observe that the value of the chemical shift δ is increased up to 0.37 mm/s showing that the pyramid completes up to octahedron. With decreasing distortion from D_5 to D_6 the value of ΔE_Q for Ln = La drops down to 0.21 mm/s. The lack of quadrupole splitting is in line with the absence of COO for this group.

In the disordered $La_{0.5}Ba_{0.5}Mn_{0.98}Fe_{0.02}O_3$ the value of ΔE_Q increases again up to 0.34 mm/s. This increase may originate from the local strains related to La and Ba randomness. The local strains are likely to increase after the [Ar-2] treatment when ΔE_Q increases up to 0.47 mm/s. This is caused by some oxygen loss, indicated by the increased lattice parameter of the cubic $Pm\bar{3}m$ phase. Finally, when the oxygen content "O_6" was restored after the [O-2] treatment the splitting ΔE_Q has regained the value characteristic of the [Dis-O] sample.

3.2.2. Sm-group of Ln's

In the oxygen-depleted series $LnBaMn_{1.96}Mn_{0.04}O_5$, both parameters of the lattice vary smoothly as the size of Ln changes (see Fig. 3, upper panel). However, we observe that the Mössbauer spectra change more drastically as we proceed from La-group to Sm-group. The area of minor doublet in the uppermost spectrum of Fig. 6 is decreased dramatically compared to the uppermost spectrum of Fig. 5. This confirms the spurious nature of the vanishing minor doublet. If this doublet is assigned to Fe^{3+} in the Mn(II) site, its disappearance must be associated to the reduction of the COO correlation length. In this situation, the ordered domains form around the Fe^{3+} dopants, which serve the anchors to pin the lattice distortions associated with COO. On the opposite, if the minor doublet originates from the Fe^{3+} ions at the COO grain-boundary site, the vanishing minor doublet would signify the reduced population of the boundaries and the growing COO correlation length.

The major doublet appears in an asymmetric form. This asymmetry was found [26] to be strongly correlated with the asymmetry expected from the preferred orientation parameters refined using FULLPROF program. This asymmetry can be removed by applying a special care to randomize the orientations of platy crystallites at the step of preparation of Mössbauer absorber or by setting the sample at magic angle at the step of measuring the spectra [26]. Since this was not always done in this work, the line intensity ratio of doublets was a free parameter at fitting the spectra.

It is observed more clearly for the Sm-group (Fig. 7) that the relative area of lines of the main doublet deviates from $\frac{1}{2}$, so that the sign of the left-to-right line area ratio deviation is changed between the "O_5" and "O_6" series. This is because the main axis of EFG (z-axis) is perpendicular to layers and $V_{zz} > 0$ in the pyramid FeO_5, but $V_{zz} < 0$ in the FeO_6 octahedron compressed along z-axis. Therefore, in the spectra of both samples [Ar-1] and [O-1] (Figs. 6 and 7), the stronger line is the transition $\pm\frac{3}{2} \rightarrow \pm\frac{1}{2}$, and the weaker line is the transition $\pm\frac{1}{2} \rightarrow \pm\frac{1}{2}$. This is in agreement with the ionic point charge model that prescribes the EFG sign and orientation along z-axis, such that $V_{zz} > 0$ for the pyramid and $V_{zz} < 0$ for the compressed octahedron [20].

In the "O_6" state, the charge and orbital order is present for the Sm-group, but absent for the La-group of Ln's. This is clearly indicated by the value of ΔE_Q, which is larger in $SmBaMn_{1.96}Fe_{0.04}O_6$ by 3.6 times than in $LaBaMn_{1.96}Fe_{0.04}O_6$. Large difference appears also in the values of distortions of the lattice cell, $D_6(Sm)/D_6(La) = 6$. Clearly, the contraction of the cell along the c-axis originates from the in-plane alignment of the active e_g orbitals of Mn^{3+}. The contraction of FeO_6 octahedron for Ln = Gd is stronger than that for Ln = Sm and this correspond to ΔE_Q increasing from 0.75 mm/s to 0.85 mm/s (Fig. 7).
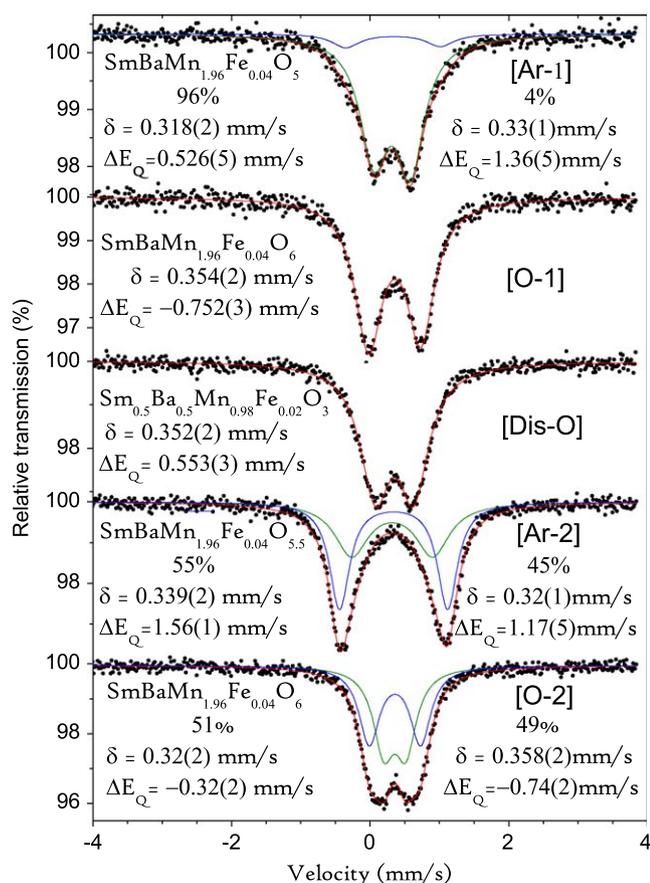
Fig. 6. Room-temperature Mössbauer spectra of $SmBaMn_{1.96}Fe_{0.04}O_6$ obtained by the sequential [Ar-1], [O-1], [Dis-O], [Ar-2] and [O-2] thermal treatments. The conditions of each step are shown in Table 1.
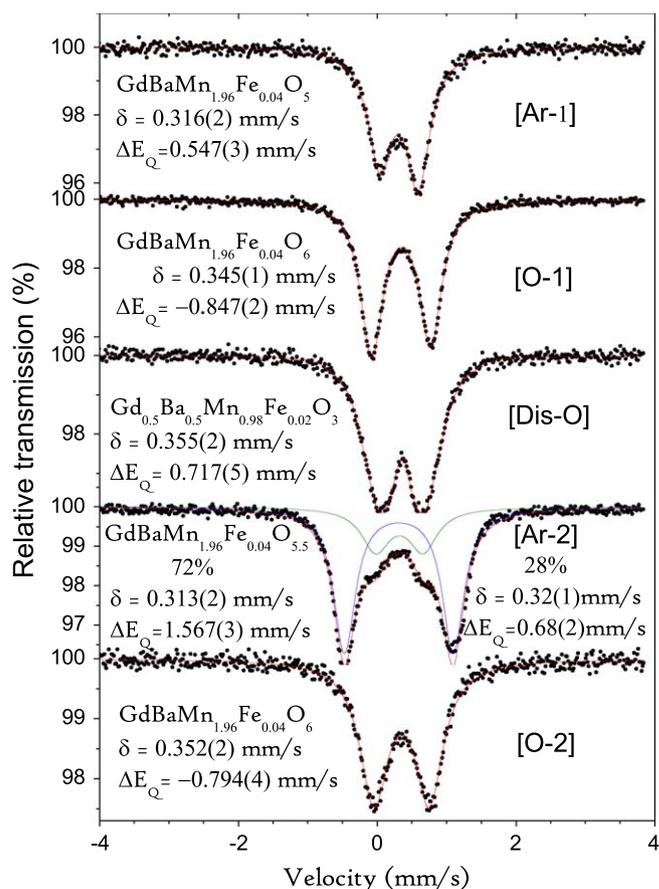
Fig. 7. Room-temperature Mössbauer spectra of $GdBaMn_{1.96}Fe_{0.04}O_6$ obtained by the sequential [Ar-1], [O-1], [Dis-O], [Ar-2] and [O-2] thermal treatments. The conditions of each step are shown in Table 1.

Among the perovskite-like cubic [Dis-O] samples the ΔE_Q value increases from Ln = La to Sm and further to Gd as 0.37, 0.55, and 0.72 mm/s, respectively. The value of ΔE_Q is sensing the increase of local distortion along with the reduction of tolerance factor. In these *A*-site disordered manganites, the Lorentzian linewidth parameter is larger than in the ordered [O-1] samples (cf., for example, 0.52 and 0.38 mm/s for Ln = Gd). This evidences the broad distribution of EFG owing to the inhomogeneity of local strains.

Mössbauer spectra of $LnBaMn_{1.96}Fe_{0.04}O_{5.5}$ were fitted with two doublets, which could be assigned to the existing sites of Mn(III) with the octahedral and pyramidal coordinations. Interatomic distances for these coordinations were reported by Caignaert et al. [6] in $LaBaMn_2O_{5.5}$ and Perca et al. [7] in $YBaMn_2O_{5.5}$. We note that the geometry of pyramid in $YBaMn_2O_{5.5}$ is close to a typical one for the JT Mn^{3+} cation. Two of the in-plane oxygens are at 1.91 Å, two others are at 1.935 Å, and the apical oxygen is at 2.1 Å. The distortion in the equatorial plane is much smaller than the apical elongation. The Fe dopant would be displaced inwards such a pyramid to equalize all five Fe–O distances. When shifted from the exact crystallographic position of a JT cation towards the pyramid apex the Fe impurity usually show the moderate ΔE_Q of the order of 0.6 mm/s [20]. This is indeed the case of minor doublet for $GdBaMn_{1.96}Fe_{0.04}O_{5.5}$ (Fig. 7). However, for the minor doublet in $SmBaMn_{1.96}Fe_{0.04}O_{5.5}$ the ΔE_Q value of 1.17 mm/s is larger. We attribute this increase of ΔE_Q to the increased distortion of the pyramid in the equatorial plane. Indeed, in $LaBaMn_2O_{5.5}$ Caignaert et al. [6] reported the in-plane interatomic distances of 1.89 and 1.96 Å.

We assign the major doublet having $\Delta E_Q = 1.56$ mm/s to the octahedral coordination, which is strongly elongated along the in-plane *a*-direction (S.G. Icma). The sign of ΔE_Q is positive, and the principal axis of EFG coincides with the *a*-axis. Despite of the equal Wyckoff octahedral and pyramidal position multiplicities, we observe that the octahedral site is more populated by the Fe dopants than the pyramidal site. Taking into account the second phase $LnBaMn_{1.96}Fe_{0.04}O_5$ (below 11% in Table 1) would only lower the population of the Fe species in the pyramidal site of the main phase. Unequal populations of these doublets are not counterintuitive because iron migrates freely between these sites

at the temperature of the [Ar-2] treatment. It must be emphasized that the mechanism of the preference of iron towards the octahedral site in the [Ar-2] samples is quite different from the mechanism of the preference of iron towards the Mn(III) site in the COO state suggested above. Namely, in the case of COO, the iron dopants cannot migrate at the temperature of the COO formation, and the preference is ensured owing to the migration of the lattice distortions associated with COO.

Final oxygenating treatment [O-2] resulted in $\Delta E_Q = 0.8$ mm/s for $GdBaMn_{1.96}Fe_{0.04}O_6$. This value is not much different from $\Delta E_Q = 0.85$ mm/s of [O-1] sample. Concomitantly, one observes a significant line broadening and a strong decrease of doublet asymmetry. Both broadening and symmetrization are caused by converting the sample into nanocrystalline form via oxygenation at the very low temperature of 350 °C. Healing the cracks induced by oxygen intercalation into orthorhombic phase $GdBaMn_{1.96}Fe_{0.04}O_{5.5}$ is prevented at such a low temperature. Orthorhombicity was previously suggested [27] to underlie the strains and cracks emerging upon the oxygen intercalation into single crystals of $GdBaMn_2O_{5.5}$. Nanostructured state of our $GdBaMn_{1.96}Fe_{0.04}O_6$ obtained by the [O-2] treatment exhibits the broadening of doublet due to surface effects in small crystallites. Basal faces of such small crystallites could be hardly aligned parallel to plane of Mössbauer absorber and the doublet becomes more symmetric.

Two $P4/mmm$ phases observed in X-ray patterns of $SmBaMn_{1.96}Fe_{0.04}O_6$ and $Sm_{0.9}Nd_{0.1}BaMn_{1.96}Fe_{0.04}O_6$ after final [O-2] treatment manifest themselves also in the Mössbauer spectra. Two doublets were assumed and the linewidths of 0.36 mm/s were obtained for both doublets having the nearly equal areas and the ΔE_Q values of -0.74 and -0.32 mm/s. Negative signs of ΔE_Q stand because of negative V_{zz} in the compressed octahedra. We note that the ΔE_Q value of the strongly split component coincide with ΔE_Q of the [O-1] sample. The splitting of weakly split component is close to ΔE_Q in $LaBaMn_2O_6$ in Fig. 5. We note that both ΔE_Q and the cell distortions D_6 in $PrBaMn_{1.96}Fe_{0.04}O_6$ and in $NdBaMn_{1.96}Fe_{0.04}O_6$ are by one and half times larger than ΔE_Q and D_6 in $LaBaMn_{1.96}Fe_{0.04}O_6$ (see the upper panel of Fig. 3). We attribute the small values of ΔE_Q and D_6 in the second phase to the absence of COO. It can be concluded that via
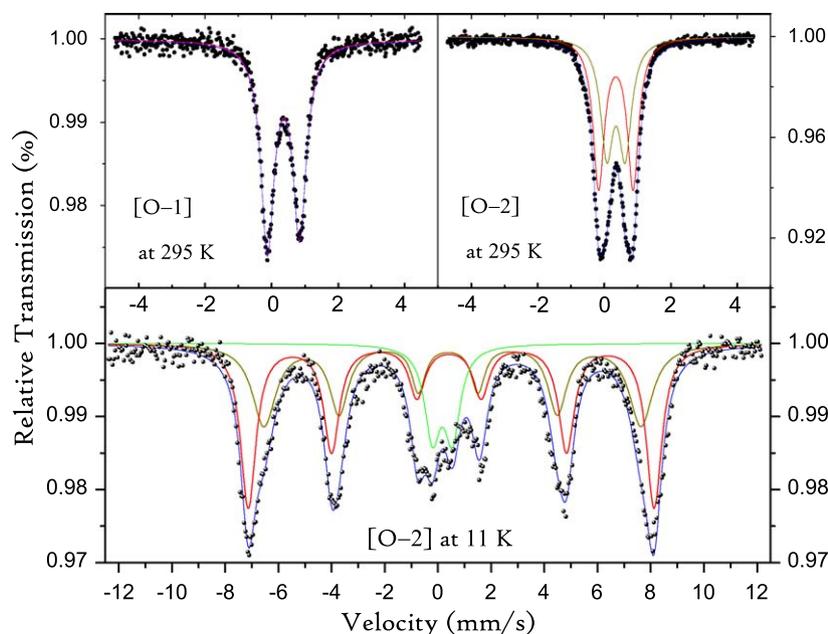

Fig. 8. Mössbauer spectra in $YBaMn_{1.96}Fe_{0.04}O_6$ for the [O-1] sample at 295 K, and for the [O-2] sample at 295 and at 11 K.

Table 2
Parameters of Mössbauer spectra in YBaMn$_{1.96}$Fe$_{0.04}$O$_6$ at two temperatures: δ-isomer shift, ε-quadrupole lineshifts in magnetic sextet[a], ΔE_Q—splitting of doublet in paramagnetic state, H_{hf}—internal magnetic hyperfine field, Θ—angle between the principal axis of electric field gradient and H_{hf}, Γ and $\Delta\Gamma$—parameters of linewidth, and %—subspectra area.

Sample	T (K)	Subspectrum	δ (mm/s)	ε (mm/s)	ΔE_Q (mm/s)	H_{hf} (kOe)	Γ[b] (mm/s)	$\Delta\Gamma$[b] (mm/s)	%
[O-1]	295	1	0.359(2)	–	−0.967(3)	–	0.482(4)	–	100
[O-2]	295	1	0.349(2)	–	−1.034(8)	–	0.410(7)	–	55
		2	0.352(2)	–	−0.55(1)	–	0.45(1)	–	45
[O-2]	11	1	0.463(6)	0.039(6)		473.1(6)	0.74(1)	0.002(3)	50
		2	0.47(1)	0.03(1)		439(2)	0.54(3)	0.037(3)	37
		3	0.16(1)	–	0.7(1)	–	0.7(1)	–	13

[a] The quadrupole lineshift ε is related to ΔE_Q via the angle Θ between V_{zz} and H_{hf} directions and the EFG asymmetry parameter η. See the work [28] for exact definition of ε.
[b] Linewidths of six lines of the sextets were fitted with two parameters Γ and $\Delta\Gamma$ assuming the constraints: $\Gamma_{1,6} = \Gamma + 2\gamma_1\Delta\Gamma \cdot H/H_0$, $\Gamma_{2,5} = \Gamma + 2\gamma_2\Delta\Gamma \cdot H/H_0$, $\Gamma_{3,4} = \Gamma + 2\gamma_3\Delta\Gamma \cdot H/H_0$, where $2\gamma_1$, $2\gamma_2$, and $2\gamma_3$ are equal to 1, 0.5789555, and 0.157911, respectively, and $H_0 = 31$ kOe/mm is the constant bringing H into velocity scale [29]. The constants γ_2, and γ_3 are given by $(g_{1/2} - g_{3/2})/(g_{1/2} - 3g_{3/2})$ and $(g_{1/2} + g_{3/2})/(g_{1/2} - 3g_{3/2})$, where $g_{1/2} = 0.181208$, $g_{3/2} = -0.103542$ are the g-factors of ground and excited states of ^{57}Fe[28].

mild oxygenation of SmBaMn$_{1.96}$Fe$_{0.04}$O$_{5.5}$ we succeeded to stabilize at room temperature (to quench) in SmBaMn$_{1.96}$Fe$_{0.04}$O$_6$ the COO-melted phase. The quenching mechanism is likely related to the formation of the nanostructured state.

3.2.3. YBaMn$_{1.96}$Fe$_{0.04}$O$_6$

In YBaMn$_{1.96}$Fe$_{0.04}$O$_6$, similarly to SmBaMn$_{1.96}$Fe$_{0.04}$O$_6$, the Mössbauer spectra of the samples [O-1] and [O-2] are different (Fig. 8). The [O-1] sample has showed a single-component spectrum. Parameters of this doublet at ambient temperature are in line with δ and ΔE_Q for other Ln's. As the size of Ln decreases in the series Sm, Gd and Y, the value of δ remains unaltered, but ΔE_Q varies from −0.75, through −0.85 to −0.97 mm/s, respectively.

On the other hand, the spectrum from [O-2] sample showed a two-doublet nature, similarly to the [O-2] sample of SmBaMn$_{1.96}$Fe$_{0.04}$O$_6$. The abundance of two components is almost equal and the difference of ΔE_Q between them is nearly twice (Table 2). The larger ΔE_Q coincides with the quadrupole splitting of the [O-1] sample. Component with a smaller ΔE_Q is again resembling to that for the quenched COO-disordered phase.

Mössbauer spectrum taken at $T = 11$ K in the [O-2] sample of YBaMn$_{1.96}$Fe$_{0.04}$O$_6$ showed that a part (13%) of ^{57}Fe species remained in paramagnetic state. Magnetically split components show the abundance ratio similar to the ratio of areas of two doublets at 295 K. From the relationship [28,29] between ΔE_Q and ε one can specify the angle between V_{zz} and H_{hf} directions. Assuming symmetric EFG we obtain the Θ values of 58(1) and 59(2) degrees for the components 1 and 2 in Table 2, respectively. However, when a significant asymmetry parameter $\eta \sim 0.8$ is allowed the ΔE_Q vs. ε relationship results in $\Theta = 90°$. Interatomic distances shown by Nakajima et al. in Fig. 7 of their work [4] suggest indeed that the EFG could be quite asymmetric. Taking the axis of major compression of the octahedra along c-axis as the principal axis of EFG, $V_{zz} < 0$, we conclude that the H_{hf} axis lies close to one of in-plane directions.

4. Concluding remarks

Room-temperature Mössbauer spectra in layered manganites evidence the high sensitivity of the electric field gradient to fine tuning of structure parameters. Although the substitution of iron for manganese suppresses the transition temperatures in each of the families of manganites, the consecution of the phase transformations is preserved. Shortening the COO correlation length is conjectured to explain the single-component spectra for the multisite structures. Indeed, Shannon ionic radii for Mn^{3+} and Fe^{3+} coincide exactly (0.645 Å), while the radius of Fe^{3+} is too small or too big for the sites of Mn(II) and Mn(IV), respectively. The fact that we frequently see the dopants in the site of Mn(III) but rarely anywhere else suggests the limited involvement of iron into the manganite electronic system. Iron stands alone not only because of stable valence but also owing to the tendency of Fe^{3+} ions to accommodate a less distorted environment matched to the isotropic configuration d^5. On the other hand, in the octahedral environment, the Fe^{3+} dopants probe faithfully the distortion of the lattice. Mössbauer spectroscopy observes the fourfold increase of the electric field gradient in the charge and orbitally ordered phases compared to the unordered ones. Finally, we proposed that the electronically unordered system can be quenched to room temperature in the nanocrystalline phase, although such a quenching was observed mainly in the two-phase samples, where the quenched melted phase coexisted with the conventional ordered phase.

Acknowledgments

References

[1] J.P. Chapman, J.P. Attfield, M. Molgg, C.M. Friend, T.P. Beales, Angew. Chem. Int. Ed. Engl. 35 (1996) 2482.
[2] F. Millange, V. Caignaert, B. Domengès, B. Raveau, Chem. Mater. 10 (1998) 1974.
[3] T. Nakajima, H. Kageyama, Y. Ueda, J. Phys. Chem. Solids 63 (2002) 913.
[4] T. Nakajima, H. Kageyama, M. Ichihara, K. Ohoyama, H. Yoshizawa, Y. Ueda, J. Solid State Chem. 177 (2004) 987.
[5] D. Akahoshi, Y. Okimoto, M. Kubota, R. Kumai, T. Arima, Y. Tomioka, Y. Tokura, Phys. Rev. B 70 (2004) 064418.
[6] V. Caignaert, F. Millange, B. Domengés, B. Raveau, Chem. Mater. 11 (1999) 930.
[7] C. Perca, L. Pinsard-Gaudart, A. Daoud-Aladine, M.T. Fernández-Díaz, J. Rodríguez-Carvajal, Chem. Mater. 17 (2005) 1835–1843.
[8] T. Nakajima, H. Kageyama, H. Yoshizawa, Y. Ueda, J. Phys. Soc. Jpn. 71 (2002) 2843.
[9] T. Nakajima, H. Yoshizawa, Y. Ueda, J. Phys. Soc. Jpn. 73 (2004) 2283.
[10] S.V. Trukhanov, A.V. Trukhanov, H. Szymczak, R. Szymczak, M. Baran, J. Phys. Chem. Solids 67 (2006) 675.
[11] R.A. Young, D.B. Wiles, Adv. X-ray Anal. 24 (1981) 1.
[12] J. Rodriguez-Carvajal, Physica B 192 (1993) 55.
[13] W.A. Dollase, J. Appl. Cryst. 19 (1986) 267.
[14] A.J. Williams, J.P. Attfield, S.A.T. Redfern, Phys. Rev. B 72 (2005) 184426.
[15] D. Akahoshi, M. Uchida, Y. Tomioka, T. Arima, Y. Matsui, Y. Tokura, Phys. Rev. Lett. 90 (2003) 177203.
[16] Y. Ueda, T. Nakajima, Progr. Solid State Chem. 35 (2007) 397.
[17] A.A. Belik, N. Hayashi, M. Azuma, S. Muranaka, M. Takano, E. Takayama-Muromachi, J. Solid State Chem. 180 (2007) 3401.

[18] T. Nakajima, H. Kageyama, H. Yoshizawa, K. Ohoyama, Y. Ueda, J. Phys. Soc. Jpn. 72 (2003) 3237.

[19] T. Nakajima, Y. Ueda, J. Alloys Compd. 383 (2004) 135–139.

[20] A.I. Rykov, A. Ducouret, N. Nguyen, V. Caignaert, F. Studer, B. Raveau, Hyperfine Interact. 77 (1993) 277.

[21] L. Er-Rakho, C. Michel, P. Lacorre, B. Raveau, J. Solid State Chem. 73 (1988) 531.

[22] V. Caignaert, I. Mirebau, F. Bourée, N. Nguyen, A. Ducouret, J-M. Greneche, B. Raveau, J. Solid State Chem. 114 (1995) 24.

[23] Yu.T. Pavlyuhin, N.G. Hainovsky, Y.Y. Medikov, A.I. Rykov, Pramana—J. Phys. 31 (1988) L445–L452.

[24] A. Rykov, V. Caignaert, N. Nguyen, A. Maignan, E. Suard, B. Raveau, Physica C 205 (1993) 63–77.

[25] F. Millange, E. Suard, V. Caignaert, B. Raveau, Mater. Res. Bull. 34 (1999) 1–9.

[26] (a) A.I. Rykov, M. Seto, Y. Ueda, K. Nomura, J. Appl. Cryst. 42 (2009) 496–501;
(b) A.I. Rykov, Y. Ueda, K. Nomura, M. Seto, Phys. Rev. B 79 (2009) 224114.

[27] A.A. Taskin, A.N. Lavrov, Y. Ando, Progr. Solid State Chem. 35 (2007) 481.

[28] A.I. Rykov, K. Nomura, Y. Ueda, A.N. Vasiliev, J. Magn. Magn. Mater. 320 (2008) 950.

[29] A.I. Rykov, V. Caignaert, G. Van Tendeloo, J.M. Greneche, F. Studer, N. Nguyen, A. Ducouret, P. Bonville, B. Raveau, J. Solid State Chem. 113 (1994) 94.